American Journal of Optics and Photonics
2024; 12(2): 18-29
http://www.sciencepublishinggroup.com/j/ajop
doi: 10.11648/j.ajop.20241202.11
ISSN: 2330-8486 (Print); ISSN: 2330-8494 (Online)

Leveraging Synthetic Data for Star and Satellite Photometry

Kimmy Chang[1, *], Alex Cabello[2], Jeff Houchard[2], Jonathan Zachary Gazak[1], Justin Fletcher[1]

[1]Space Systems Command (A&AS), Kihei, Hawaii, U.S.
[2]EO Solutions, Kihei, Hawaii, U.S.

Email address:

kimmychang@odysseyconsult.com (Kimmy Chang), alex.cabello@e-o.solutions (Alex Cabello), jeff.houchard@e-o.solutions (Jeff Houchard), jonathangazak@odysseyconsult.com (Jonathan Zachary Gazak), justinfletcher@odysseyconsult.com (Justin Fletcher)
[*]Corresponding author

To cite this article:

Kimmy Chang, Alex Cabello, Jeff Houchard, Jonathan Zachary Gazak et al. (2024). Leveraging Synthetic Data for Star and Satellite Photometry. *American Journal of Optics and Photonics, 12*(2), 18-29. https://doi.org/10.11648/j.ajop.20241202.11

Received: 16 August 2024; **Accepted:** 4 September 2024; **Published:** 29 September 2024

Abstract: In the realm of Space Domain Awareness (SDA), precise photometric measurements are essential for applications such as stability analysis, shape recovery, and material studies of satellites. However, current methods that rely on manual data collection and analysis are not scalable to autonomous frameworks, which are increasingly necessary due to the growing congestion in space. This research presents an approach to automate photometric measurements within a network of telescopes operating in non-ideal conditions. Our work focuses on achieving reliable photometry in degraded weather conditions, where traditional methods might fail, leading to false detections and unnecessary follow-up efforts. We utilize the SatSim space scene simulator to generate synthetic data for training and testing photometry algorithms. These algorithms include both traditional aperture photometry and machine learning-based approaches. Our methodology employs dynamic segmentation techniques to optimize the detection of satellites and stars under various adverse conditions. The segmentation methods were evaluated for their robustness in different scenarios, with the Depth-First Search + Interquartile Range (DFS + IQR) approach showing the most promise. Through extensive experimentation, we demonstrate that our approach can achieve a photometric precision of approximately 10^{-1}, even in adverse conditions. This represents a significant advancement in the field, as it enables more reliable satellite detection and tracking in real-world, non-photometric environments. Additionally, our ablation studies highlight the importance of balanced datasets in reducing error metrics, particularly for underrepresented satellite classes. This work contributes to the development of more effective autonomous SDA systems, capable of operating efficiently in a wide range of environmental conditions.

Keywords: Aperture Photometry, Machine Learning, Visual Magnitude, Synthetic Data

1. Introduction

The applications of photometry in Space Domain Awareness (SDA) include stability analysis [1], shape recovery [2], and size and materials studies [3, 4]. Proper measurement of the input photometric data into these tools determines the quality of output information. Typically, such studies involve manual collection, reduction, and analysis of small sets of data on one or few targets. These narrow studies do not scale to autonomous frameworks and limit the applicability of the statistical techniques to the increasingly congested space environment.

Automatic and general photometric measurements facilitate the extraction of useful data from routine catalog maintenance missions and enhance efficiency within autonomous networks. While overall sensor characterization can assess ideal telescope performance, SDA telescopes seldom operate under such optimal "photometric" conditions. Furthermore, the quality of astronomical observations is expected to decline further in the future [5]. The SDA mission set prioritizes temporal and spatial coverage over extreme scientific precision. In non-photometric conditions, the effective performance of telescopes is compromised by factors such as observing location and pointing (extinction), local weather conditions (e.g., cloud cover and turbulence), and changes in equipment over time (e.g., dust accumulation and

periodic cleaning).

In the astronomical sciences, precision photometry is calculated only in pristine conditions, and telescopes tend to be used for different experiments in "non-photometric" weather. Detection and measurement of on-orbit assets is critical even in degraded weather conditions. In conditions causing degraded performance relative to measured system zero point, automated photometry is critical: An object may sink below the actual zero point of a system and be flagged as missing when, in fact, it is simply too dim to be observed given actual conditions. This situation drives unnecessary follow-up search and recovery efforts which consume cycles in autonomous systems and can create false alerts to operators and decision makers.

In pristine photometric weather and carefully controlled experiments, astronomers can achieve better than 10^{-3} photometric accuracy from the ground and 10^{-5} from space [6–8]. These levels of precision are costly in exposure time, experiment design, and data analysis. In this work we demonstrate $\sim 10^{-1}$ photometric precision in an autonomous telescope network operating in adverse weather conditions and tuned to maximize source detections in minimized exposure times.

2. Related Works

The application of neural networks to the problem of detecting satellites in high contrast ground-based telescope images has spawned the field of learned SDA [9]. The underlying models applied and training techniques have been explored and optimized since [10–12], driving enhanced detection performance. Automatic detection of stars [13] provides the necessary astrometric information to convert pixel locations to on-sky coordinates and measure the orbits of objects detected. The combined algorithms enabled this work; by aligning stars with astrometric catalogs, the counts collected from field stars enable automatic derivation of the photometric system and application of that zero point to determine the magnitudes of detected satellites.

The Kepler satellite, designed to detect transiting exoplanets, regularly achieves $\sim 10^{-5}$ photometric precision [7]. From the ground, astronomers have achieved $\sim 10^{-4}$ on two meter apertures using specialty orthogonal transfer Charge-Coupled Devices (CCDs) and novel Point Spread Function (PSF) shaping techniques [8, 14, 15].

3. Approach

3.1. Data

SatSim is a high-fidelity, modular, Graphics Processing Unit (GPU)-accelerated space scene simulator developed to support the detection of Resident Space Objects (RSOs) using machine learning. It focuses on creating large volumes of annotated electro-optical imagery, which is useful for training, improving, and validating RSO detection models. SatSim's capabilities include generating synthetic images of satellite breakups and other rare or complex events, making it an invaluable tool for SDA research and testing. Figure 1 shows the SatSim scene generation pipeline.

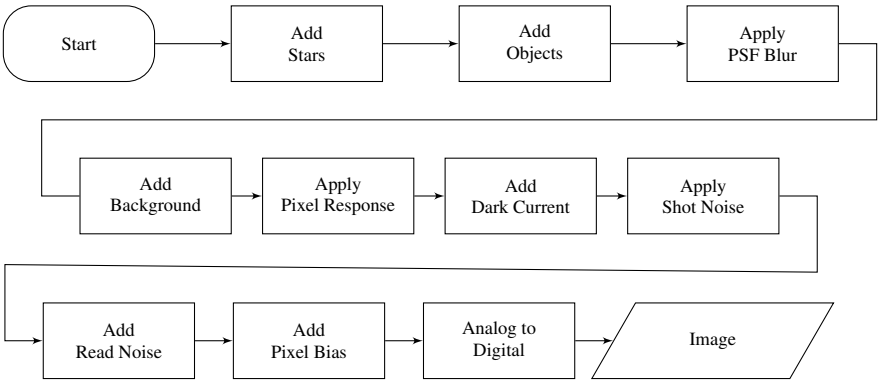

Figure 1. *SatSim Scene Generation Pipeline. Each pipeline stage is configurable with input parameters, allowing users to easily configure a static, procedural, or random sample simulation.*

SatSim was used in this experiment to procedurally generate synthetic data for the training and testing of machine learning models and traditional photometry algorithms. This dataset includes raw synthetic images and ground-truth photometry annotations for RSOs and stars. Examples from the dataset are shown in Figure 2.

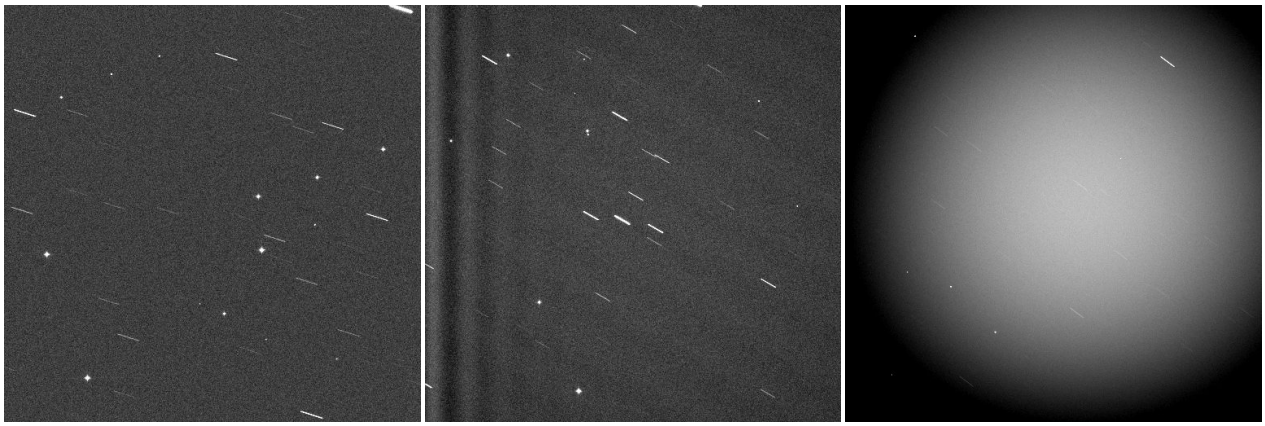

(a) *(b)* *(c)*

Figure 2. *Examples from the dataset: (a) an image with no fixed pattern noise and no stray light; (b) an image with fixed pattern noise; (c) an image with stray light.*

The synthetic data were modeled from two Raven-class telescopes. The simulation parameters are detailed in Table 1.

Table 1. *SatSim scene generation parameters for learned photometry dataset.*

Parameter	Observatory 1	Observatory 2
Spatial Oversampling Factor	15	15
Field-of-View (FOV)	0.3 degrees	0.3 degrees
Pixels	512x512	1024x1024
Dark Current	0	0
Gain	1	1
Bias	0	0
Zero Point	21.5	22.1
Analog-to-Digital (A2D) Response	Linear	Linear
A2D Gain	1.5	1.5
A2D Bias	1000	1000
Read Noise	9 e-	9 e-
PSF Mode	Physical Optics Propagation	Physical Optics Propagation
Aperture Diameter	0.4 m	0.4 m
Atmosphere	None	None
Exposure Time	U([1, 2, 3, 4, 5]) sec	U([1, 2, 3, 4, 5]) sec
Images per Subset	6	6
Background	U(17.5, 22.5) mv	U(17.5, 22.5) mv
Stray Light	U(On, Off)	U(On, Off)
Stars	SSTRC7 Catalog	SSTRC7 Catalog
Objects per Image	U(10, 20)	U(10, 20)
Object Apparent Magnitude	U(9.0, 18.5)	U(9.0, 18.5)
Total Images	24,000	24,000

3.2. The Method

The inputs to our photometry pipeline are FITS files that contain astronomical images representing observed data, calibration information (sensor gain and exposure time), and annotations (star and satellite bounding box and centroid coordinates). The images are stored as a two-dimensional array of pixel values, where each pixel value corresponds to a digital number (DN) count. These DN counts provide a quantification of the detected signal at each pixel in the image. These inputs serve as the foundation for our subsequent feature extraction process.

To facilitate feature extraction, we employ a segmentation method detailed in Section 3.3. This segmentation method extracts DN counts for stars and satellites' aperture, annulus, and background regions. These regions are defined based on

the bounding box and centroid coordinates associated with each target.

To derive relevant physical parameters using aperture photometry, we apply the following formula:

$$\text{flux} = \frac{\text{apt} - r \times \text{ann}}{g \times t}$$

Here, apt and ann represent the sums of DN counts within the aperture and annulus, respectively; g is the sensor's gain; r represents the ratio of the area between the aperture and annulus; and t is the exposure time. We then calculate the instantaneous magnitude,

$$m_{\text{inst}} = -2.5 \log (\text{flux})$$

Next, we estimate the zero point, with the equation:

$$\text{Zero Point} = \text{VM}_{\text{catalog}} - m_{\text{inst}}$$

Here, $\text{VM}_{\text{catalog}}$ corresponds to the visual magnitude obtained from the catalog.

For our learned approaches, we input the following features into our models: apt, ann, g, t, r, obj type. Here, the obj type is satellite or star. We found that this indicator variable significantly helped with the data imbalance between stars and satellites in our dataset. The overall pipeline for our method is shown in Figure 3.

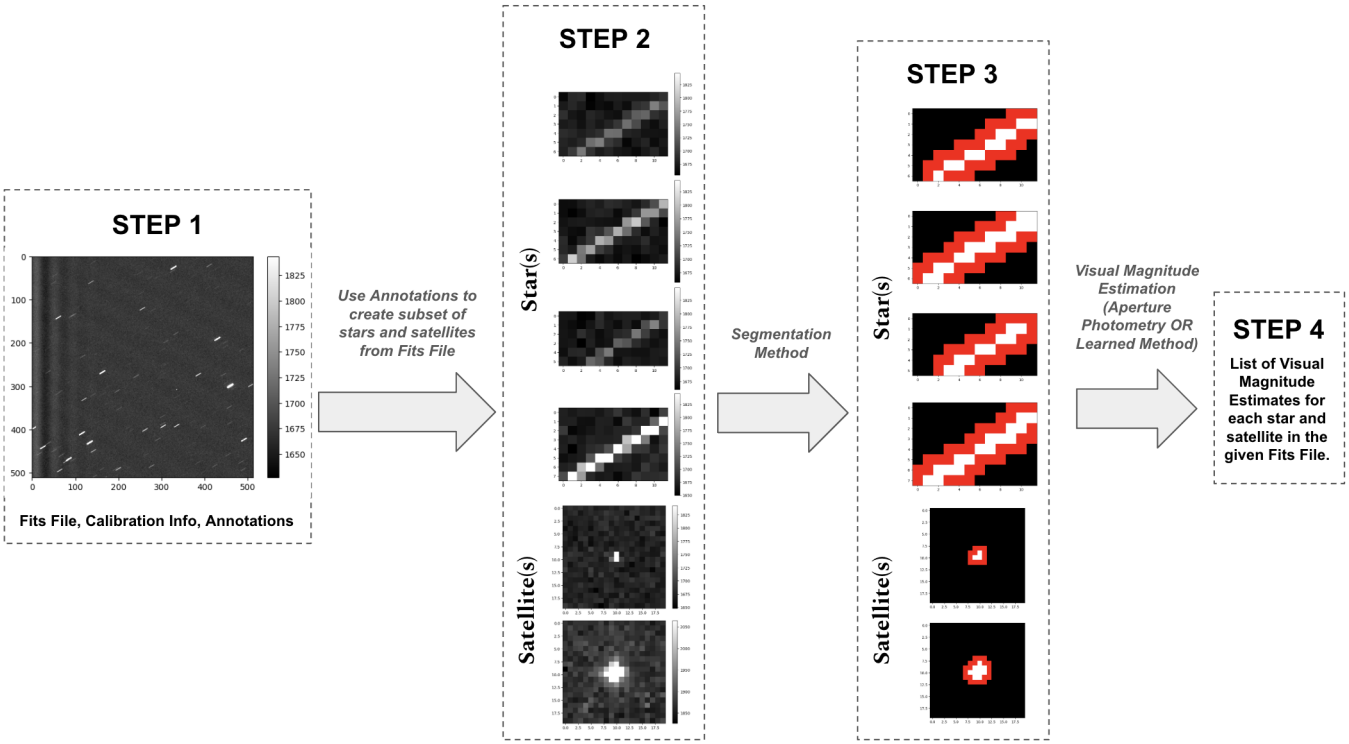

Figure 3. *Overview of the photometry method pipeline. Each Fits file is accompanied by calibration information and annotations for stars and satellites. The pipeline involves parsing out individual stars and satellites from the image, segmenting the aperture and annulus regions for each object, and generating visual magnitude estimates for stars and satellites within the Fits file.*

3.3. Segmentation Methods

We assessed three segmentation threshold techniques: Mean, Interquartile Range (IQR), and Depth-First Search + Interquartile Range (DFS + IQR). The Mean threshold method identifies aperture pixel locations where the DN count exceeds the mean DN count of the bounding box frame, multiplied by a dynamic threshold. The IQR threshold method defines the aperture as pixel locations with DN count surpassing a dynamic threshold calculated from the IQR. The DFS + IQR threshold approach utilizes prior knowledge of target placement, initiating from the center pixel and expanding outward based on an upper dynamic threshold derived from the IQR. Notably, we considered other search algorithms like breadth-first and greedy search but found DFS to be the most accurate and memory-efficient solution.

Each of these methods delineates an annulus by identifying pixels surrounding the aperture while categorizing the remaining pixels as background. The segmentation results are depicted in Figure 4. Qualitatively, the DFS + IQR method demonstrated the greatest robustness in handling noise and clustered stars/targets in the reference frame. As a result, we selected this threshold technique as our primary segmentation method. The overall algorithm is outlined in Figure 1. Notably, the dynamic threshold determines the tightest aperture and

annulus bounds by initially setting the threshold at 2.5 and iteratively decreasing it by 0.1 until reaching 0.0. From Figure 5, it is evident that lower thresholds tend to capture higher levels of noise and off-centered target and star cases, while the highest IQR threshold yields the most accurate segmentation. Figure 6 illustrates how the aperture region expands as the IQR threshold decreases.

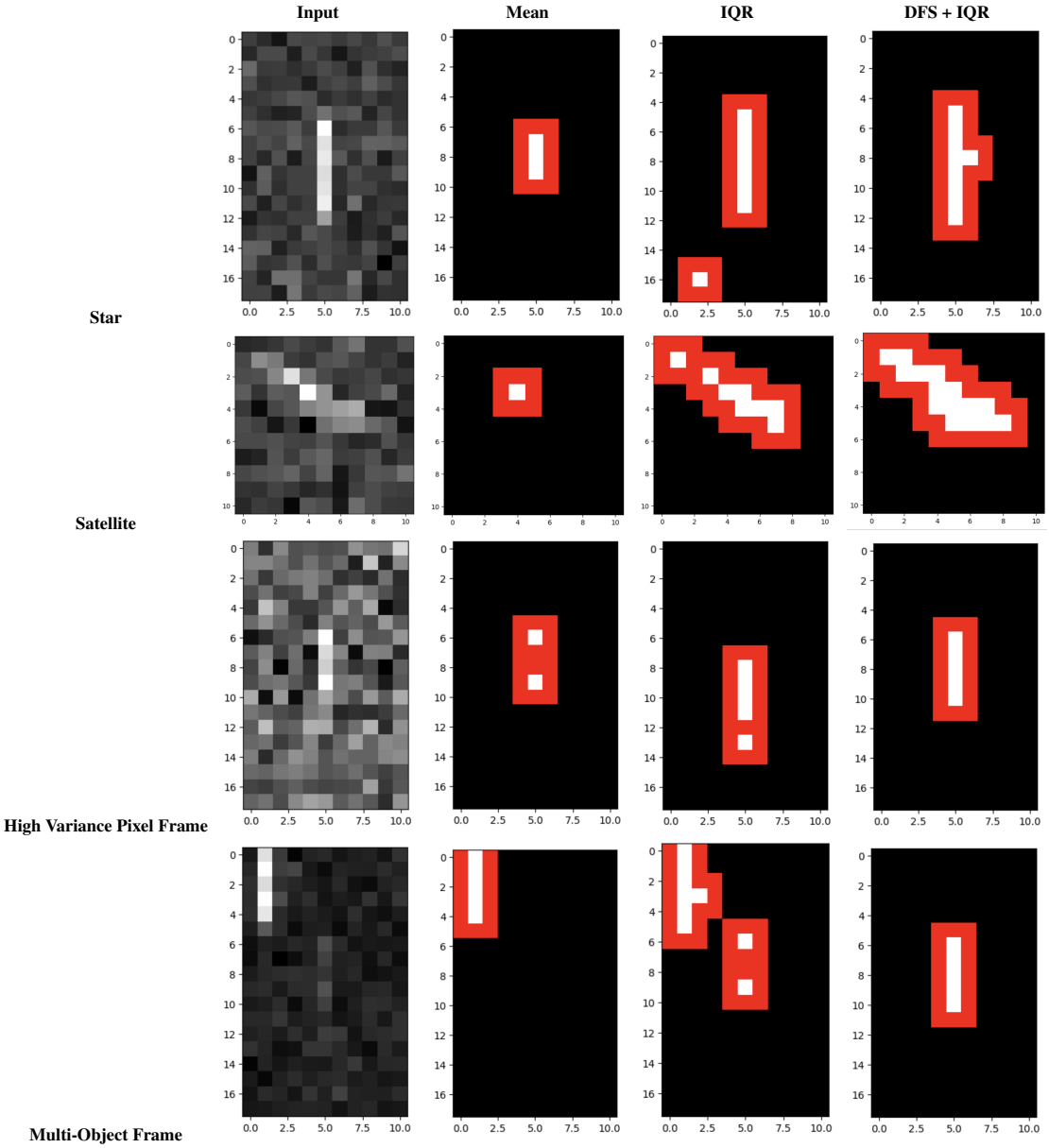

Figure 4. *Visual representation of segmentation thresholds. The mean threshold frequently results in an underestimation of the aperture region, while the IQR threshold tends to include additional pixels, typically those with a high DN count. The combination of DFS and IQR consistently produces segmentation results that closely resemble the visual aperture regions.*

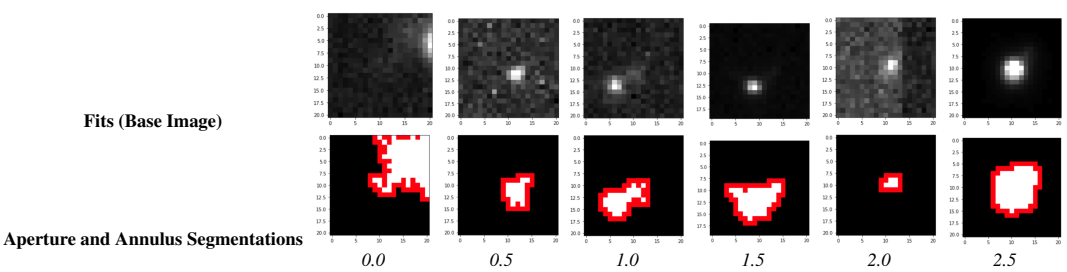

Figure 5. *Visual examples illustrating aperture (white), annulus (red), and background (black) segmentation cases for stars across the dynamic IQR threshold range from 0.0 to 2.5 at 0.5 increment steps.*

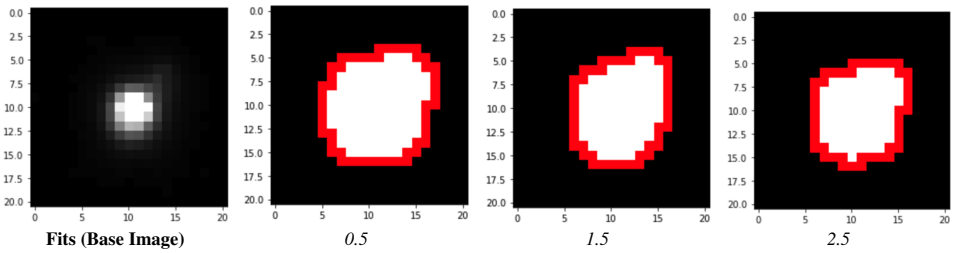

Figure 6. *The aperture segmentation region expands as the threshold increases from 0.5 to 1.5 to 2.5.*

Algorithm 1: Segmentation Algorithm "IQR + DFS"

Data: Input data: .fits, centroid of star/target x_{center}, y_{center}
Result: Output apt and ann
for *each star and satellite* s *in .fits* **do**
  Define bounding box area for star as ± 10 pixels from center coordinates (x_{center}, y_{center}).
  Store DN counts in list s_{DN}.
  Define Aperture
  for *threshold* t_{IQR} *in range(2.5, 0.0, -0.1)* **do**
    if *len(apt)* > 0 *and len(ann)* > 0 *and* $flux > 0$ **then**
      break
    end
    else
      Run DFS$_{aperture}(t_{IQR}, s_{DN})$ to add neighboring pixels from starting centroid (x_{center}, y_{center}) to aperture list.
    end
  end
  Define Annulus
  Add the pixels 1-pixel around the aperture to the annulus list.
end

Algorithm 2: DFS$_{aperture}(t_{IQR})$ Algorithm

Data: Input data: t_{IQR}, s_{DN}, .fits, centroid of star/target x_{center}, y_{center}
Result: Output list of aperture coordinates
Define $t_{threshold} = Q_3 + t_{IQR} * (Q_3 - Q_1)$ where Q_3 and Q_1 are first and third quartiles in s_{DN}, respectively.
if $DN_{(x,y)} < t_{threshold}$ **then**
  o
end
r visited or outside of bounding box return aperture list
else
  mark (x, y) as visited
  add (x, y) to aperture list
  for *all bordering pixels to* x, y **do**
    DFS$_{aperture}(t_{IQR})$
  end
end

3.4. Metrics

We conduct a comprehensive assessment of our method's effectiveness through both qualitative and quantitative analysis. Our qualitative evaluation involves a visual examination of aperture and annulus segmentation quality. For quantitative analysis, we employ three established performance metrics: error, mean absolute error (MAE), and mean percent error. The disparity between estimated/predicted values and true values is gauged by the error, as expressed in the equation below.

$$\text{Error } = y_i - x_i$$

where y_i is the true value and x_i is the estimated value. Individual estimation errors are computed to discern potential underestimation or overestimation tendencies of the method.

Mean absolute error is computed as follows:

$$\text{Mean absolute error } = \frac{1}{n}\sum_{i=1}^{n}|y_i - x_i|$$

where n denotes the total count of targets within the pertinent dataset.

Percent error serves as the established photometry measure for evaluating the error of visual magnitudes, enabling a straightforward appraisal of estimated values against expected values. The mean percent error is determined using the subsequent formula:

$$\% \text{ error } = \sum_{i=1}^{n}\frac{|y_i - x_i|}{x_i} \times 100\%$$

The aforementioned metrics are employed for quantitative performance assessment of our methodologies. Error functions as a foundational performance baseline. While absolute error introduces a measure of deviation magnitude, percent error provides relative accuracy information, albeit with limitations when expected values approach zero or are very small.

4. Experiments

4.1. Synthetic Data

We investigate traditional aperture photometry and learned photometry techniques. Our approach utilizes DFS + IQR

with dynamic thresholds to delineate aperture and annulus regions for all celestial objects. Expanding on the foundation of Aperture Photometry, we integrate key variables such as the sum and ratio of aperture and annulus regions, along with gain and exposure time, as pivotal features in five machine learning methods: Multilayer Perceptron (MLP), 1-Dimensional CNN (Conv1D), K-Nearest Neighbors (KNN), XGBoost, and Random Forest. The number of stars and satellites for both RME02 and RME03 used in training[1] and validation are specified in Table 2.

Table 2. *Synthetic Dataset Size Details.*

		Stars		Satellites	
Type	**Method**	**Train**	**Validation**	**Train**	**Validation**
Stray Light	RME02	452,451	113,073	9,241	2,351
	RME03	239,352	59,897	4,794	1,140
No Stray Light	RME02	64,604	16,175	1,782	422
	RME03	7,714	1,922	317	86

Our findings show that the Random Forest learned approach has notably low error rates, as seen in Table 3. Error metrics are calculated for a prespecified holdout dataset. Notably, Random Forest achieves error metrics four to five times lower than traditional Aperture Photometry. Interestingly, Random Forest, XGBoost, and KNN all surpass the performance of traditional aperture photometry. In addition to this, we observe lower error metrics for satellites compared to stars in Random Forest, especially with the RME03 sensor. In Figure 7, we see that error metrics for both stars and satellites have less variability about zero in both training and validation sets with Random Forest compared to Aperture Photometry. However, both methods struggle with dimmer objects, especially stars with a true visual magnitude exceeding 12.

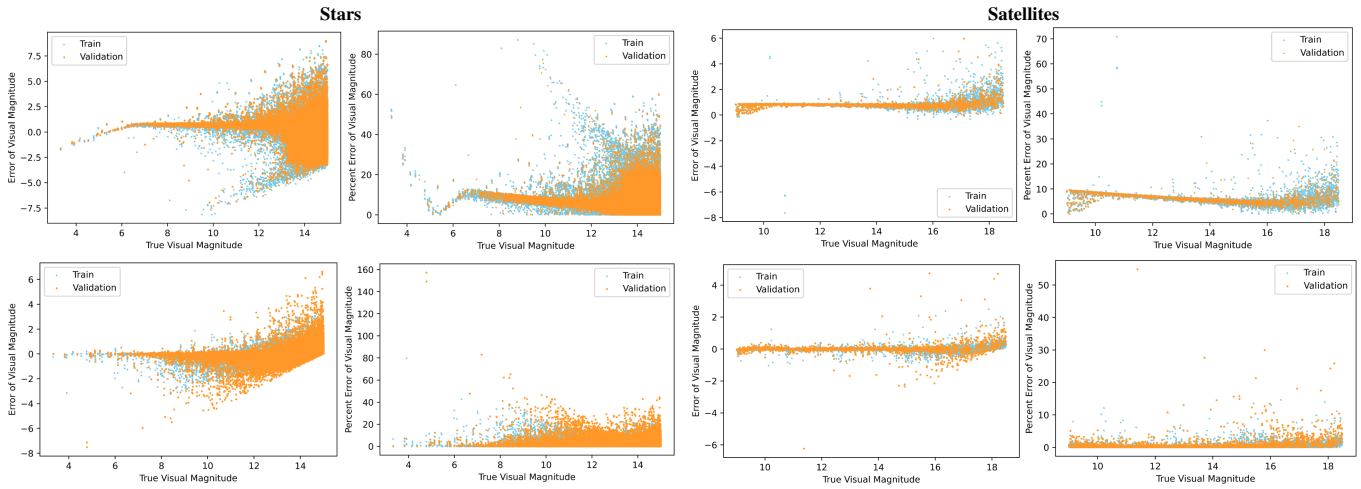

Figure 7. *Error Metric Plots for RME02 No Stray Light Case. The plots in Row 1 and Row 2 correspond to Aperture Photometry and Random Forest, respectively. Error metrics for stars and satellites exhibit less dispersion around zero in the Random Forest method compared to traditional Aperture Photometry*

For our more challenging stray light case, we observe a similar superiority of Random Forest to traditional Aperture Photometry (see Table 4). We observe a similar phenomenon where satellite error metrics are less than that of stars amidst the data imbalance between the classes of stars and satellites.

[1] We use the "training" dataset to estimate zeropoint for Aperture Photometry.

Table 3. *No Stray Light Photometry Results of Stars and Satellites for RME02 and RME03. Error metrics for visual magnitude estimation are four to five times lower with the Random Forest model compared to traditional Aperture Photometry.*

		Stars		Satellites	
Sensor	**Method**	**MAE**	**% Error**	**MAE**	**% Error**
RME02	MLP	25.8505	208.4858	19.2444	178.6538
	Conv1D	0.9315	7.4103	2.3246	18.0245
	Aperture Photometry	0.8575	6.2494	0.8230	6.1725
	KNN	0.4108	3.0931	0.9021	5.9698
	XGBoost	0.2453	1.8227	0.2504	1.7426
	Random Forest	*0.2157*	*1.5973*	*0.1689*	*1.1127*
RME03	MLP	117.0065	117.0065	116.8431	941.7750
	Conv1D	0.9199	7.2971	2.3291	17.8293
	Aperture Photometry	1.2411	9.1705	1.3324	10.1006
	KNN	0.3627	2.7017	0.8370	5.5195
	XGBoost	0.2127	1.5808	0.2101	1.4817
	Random Forest	*0.1949*	*1.4365*	*0.0986*	*0.6463*

Table 4. *Stray Light Photometry Results of Stars and Satellites for RME02 and RME03. The Random Forest model exhibits significantly lower mean absolute error and percent error metrics compared to traditional Aperture Photometry.*

		Stars		Satellites	
Sensor	**Method**	**MAE**	**% Error**	**MAE**	**% Error**
RME02	Aperture Photometry	0.8940	6.6567	0.9242	6.8881
	Random Forest	*0.3317*	*2.4987*	*0.2986*	*2.0733*
RME03	Aperture Photometry	1.2025	9.2048	1.2187	9.5568
	Random Forest	*0.3766*	*2.9189*	*0.2236*	*1.5277*

4.2. Ablation Studies

We utilized our largest synthetic dataset subset, denoted as RME02 with stray light, for conducting our ablation studies. It is noteworthy that throughout variations in the training dataset, encompassing changes in parameters such as composition and size, we maintained a consistent count of stars and satellites in our validation dataset, specifically comprising 113,073 stars and 2,351 satellites.

4.2.1. Equal Star-to-Satellite Classes

In our original dataset, the train and validation datasets consist of approximately 98% stars and 2% satellites. Consequently, the zero point estimation in Aperture Photometry and the Random Forest model may exhibit signs of overfitting toward the star class. To address this issue, we equalize the number of stars and satellites in the dataset while maintaining the original validation dataset. As shown in Table 5, balancing the number of stars and satellites consistently leads to lower error metrics for both classes in Aperture Photometry, nearly halving the Mean Absolute Error and Percent Error for the satellite class. However, for our Random Forest model, we observe only marginal improvements in satellite error metrics while experiencing a substantial increase in star error metrics.

Table 5. *Maintaining an equal number of stars and satellites in the training dataset is crucial for Aperture Photometry. In contrast, Random Forest demonstrates greater robustness to the significant class imbalance between stars and satellites. Note: all error metrics are for validation.*

			Stars		Satellites	
Method	**# Train Stars**	**# Train Satellites**	**MAE**	**% Error**	**MAE**	**% Error**
Aperture Photometry	452,451	9,241	0.8575	6.2494	0.8230	6.1725
	9,241	9,241	*0.7868*	*5.5918*	*0.4214*	*3.1233*
Random Forest	452,451	9,241	*0.2157*	*1.5973*	0.1689	1.1127
	9,241	9,241	0.2850	2.1482	*0.1464*	*0.9786*

4.2.2. Star-Only Training

We initiate our analysis with a star-only training dataset containing 452,451 stars. As illustrated in Figure 8, the Random Forest model demonstrates a need for a minimum of 50 satellites in its training dataset to outperform the error metrics of Aperture Photometry. Furthermore, we observe that the error metrics for stars and satellites in the Random Forest model become comparable after incorporating approximately 4,000 satellites into the training dataset.

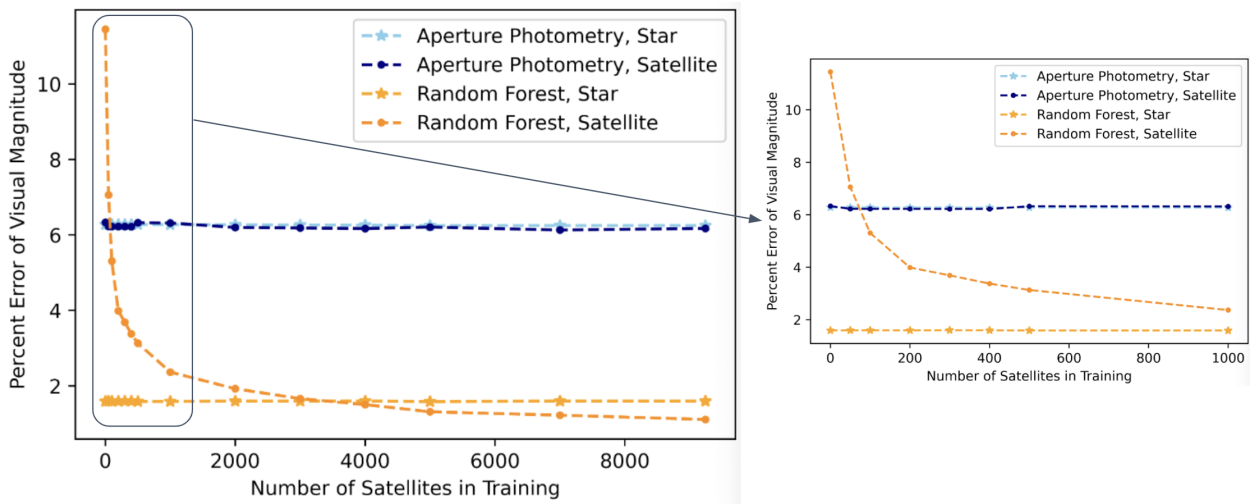

Figure 8. Aperture Photometry maintains consistent performance in the absence of satellite training data. Random Forest, however, requires 50 satellites in training to surpass Aperture Photometry.

4.3. Real Data

Across 97 Fits files, we recover approximately 130,000 annotated stars. It is noteworthy that the visual magnitude dataset exhibits a negatively skewed distribution, with a central tendency around 17, as illustrated in Figure 9.

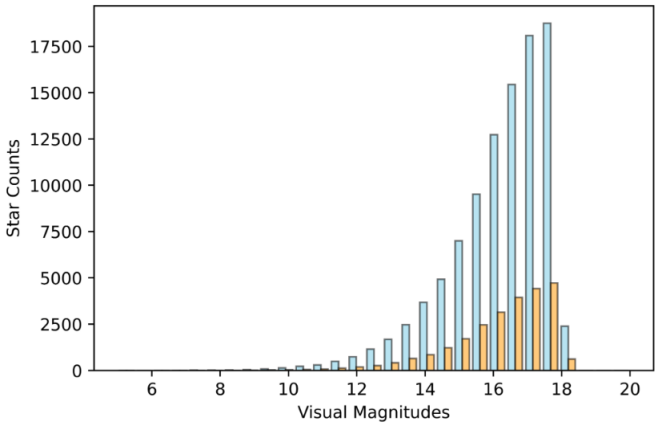

Figure 9. Negative skew distribution of visual magnitudes in the Rate Sidereal dataset.

Table 6. Validation error metrics for Random Forest are approximately three times lower than those for Aperture Photometry. While the error metrics for Aperture Photometry remain comparable between train and validation sets, they double for Random Forest.

	Train		Validation	
Method	**MAE**	**% Error**	**MAE**	**% Error**
Aperture Photometry	0.7477	4.6353	0.7488	4.6463
Random Forest	*0.1000*	*0.6231*	*0.2603*	*1.6219*

Consistent with our synthetic results, the Random Forest Method exhibits error metrics nearly three times lower than those of Aperture Photometry (see Table 6). Figure 10 demonstrates that our methods excel particularly with brighter stars, as the magnitude of error increases with visual magnitude.

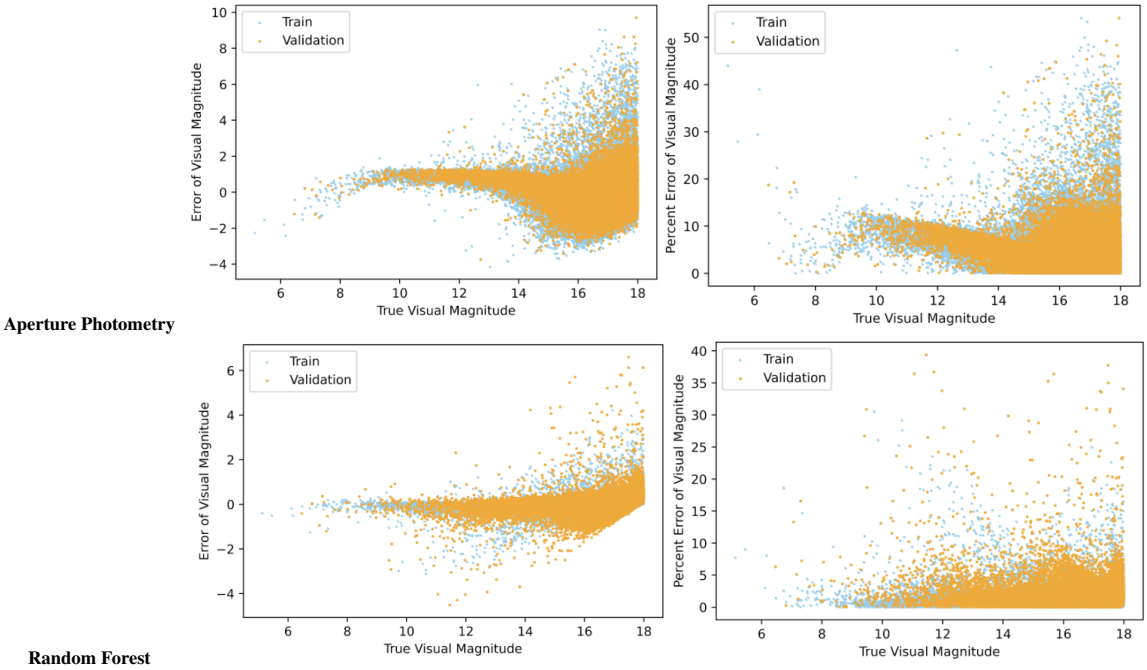

Figure 10. *Error tends to be higher around the central tendency of the dataset. Additionally, we notice that the error is lowest for the brightest stars in the dataset.*

We further examined the performance of our methods across dynamic IQR thresholds. As illustrated in Figure 11, the Random Forest method consistently maintains high performance across various IQR thresholds, whereas Aperture Photometry demonstrates variable performance, particularly at the extremes of our IQR thresholds. Subsequently, we investigated the impact of training dataset size, with our holdout set comprising a constant size of 24,990 stars. Figure 12 reveals that Aperture Photometry's zero point estimations require only a few samples, while Random Forest achieves superior performance after a mere 50-star sample. Notably, Random Forest exhibits a percent error of less than two and maintains relatively stable performance after only 10,000 star samples.

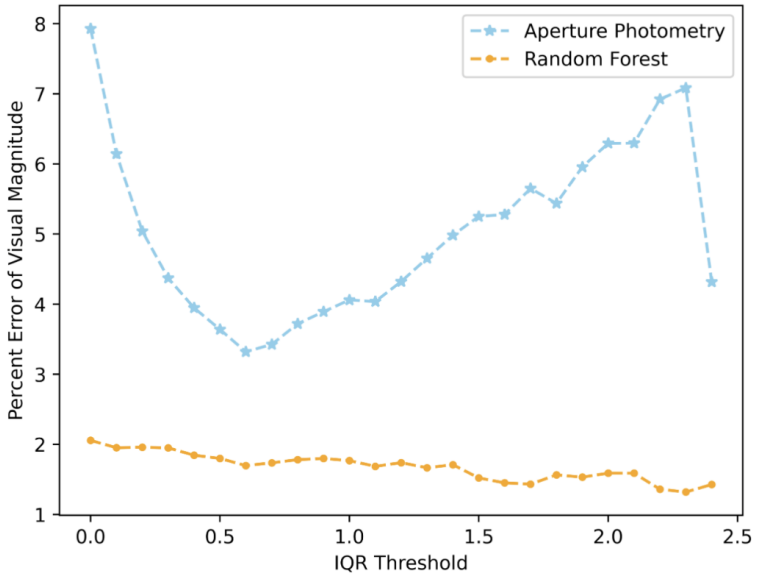

Figure 11. *Constant and Variable Performance of Random Forest and Aperture Photometry across Dynamic IQR Thresholds, respectively.*

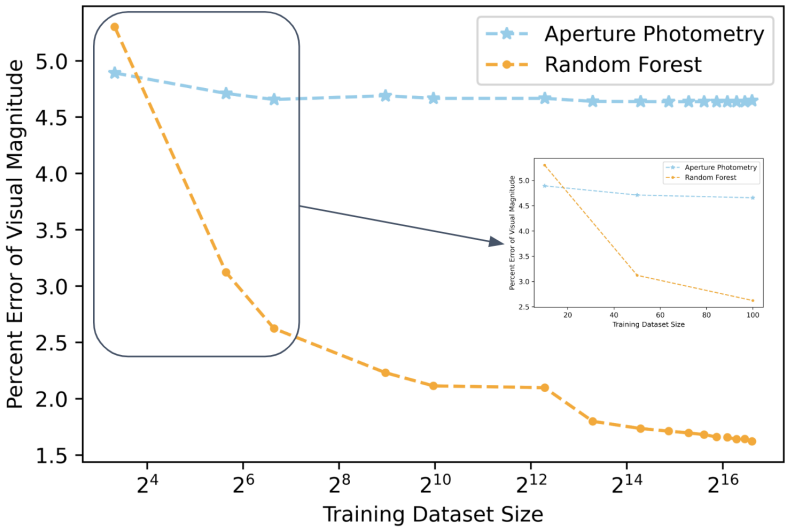

Figure 12. *Random Forest surpasses Aperture Photometry after only 50 training samples, with marked improvements observed as the dataset size increases. In contrast, Aperture Photometry's performance plateaus early on.*

5. Conclusion

Detecting and measuring on-orbit assets is crucial even in degraded weather conditions. Automated photometry is imperative in such conditions, as objects may fall below the system's zero point and be erroneously flagged as missing due to dimness under actual conditions. This situation leads to unnecessary search and recovery efforts and can generate false alerts for operators and decision-makers.

We present a novel approach to traditional aperture and annulus segmentation methods, defining pixel-specific regions and leveraging them in both traditional aperture photometry and a learned approach to visual magnitude estimation for stars and satellites.

We contribute synthetic datasets, including both no stray light and stray light cases, annotated for two different sensors with over 500,000 stars and 10,000 satellites, as well as a real dataset with annotations for over 125,000 stars and visual magnitudes. For synthetic data, we achieve an impressive visual magnitude percent error of 2.50% and 2.07% for stars and satellites, respectively, in challenging stray light scenarios. When tested on real on-sky rate sidereal data, our method demonstrates a percent error of 1.62%.

Our methods adeptly address data imbalances between stars and satellites, achieving outstanding performance in visual magnitude estimation even with a modest training dataset of only 100 stars. We present our research as a foundational framework for future endeavors in learned photometry and anticipate the growing significance of our approach in meeting the escalating demand for automated photometry.

Acknowledgments

The authors would like to thank the 15th Space Surveillance Squadron for access to AEOS data. The views and conclusions contained in this document are those of the authors. They should not be interpreted as representing the official policies, expressed or implied, of the United States Air Force or the U.S. Government.

ORCID

0009-0000-3361-3493 (Kimmy Chang)

Author Contributions

Kimmy Chang: Conceptualization, Formal Analysis, Investigation, Methodology, Project administration, Resources, Software, Validation, Visualization, Writing - original draft, Writing - review & editing

Alex Cabello: Data curation

Jeff Houchard: Funding acquisition, Supervision

Jonathan Zachary Gazak: Supervision, Writing ¨C original draft, Writing - review & editing

Justin Fletcher: Funding acquisition, Supervision, Writing - original draft, Writing - review & editing

Conflicts of Interest

The authors declare no conflicts of interest.

References

[1] Abercrombie, M. D., Calef, B., and Naderi, S., "Light Curve Analysis of Deep Space Objects in Complex Rotation States," (2021).

[2] Balster, P., Jones, G., Hofer, G., Newsom, D., and Frueh, C., "Object Characteristic Determination Using Brightness Measurements," (2023).

[3] Gazak, J. Z., Swindle, R., Phelps, M., and Fletcher, J., "Simultaneous Detection, Recognition, and Localization of Geosynchronous Satellites from Ground Based Imagery," (2023).

[4] Pearce, E. C., Krantz, H., Block, A., Sease, B., and Kirshner, M., "Rapid Discrimination of Resident Space Objects Using Near-Infrared Photometry," (2021).

[5] Vidale, C. H. M.-E. D. B.-O. D. M. S. P. L., "Impact of climate change on site characteristics of eight major astronomical observatories using high-resolution global climate projections until 2050," Astronomy and Astrophysics (August 2022).

[6] Mann, A. W., Gaidos, E., and Aldering, G., "Ground-Based Submillimagnitude CCD Photometry of Bright Stars Using Snapshot Observations," Publications of the Astronomical Society of the Pacific 123(909), 1273-1289 (2011). Publisher: [The University of Chicago Press, Astronomical Society of the Pacific].

[7] Koch, D. G., Borucki, W. J., Basri, G., Batalha, N. M., Brown, T. M., Caldwell, D., Christensen-Dalsgaard, J., Cochran, W. D., DeVore, E., Dunham, E. W., Gautier III, T. N., Geary, J. C., Gilliland, R. L., Gould, A., Jenkins, J., Kondo, Y., Latham, D. W., Lissauer, J. J., Marcy, G., Monet, D., Sasselov, D., Boss, A., Brownlee, D., Caldwell, J., Dupree, A. K., Howell, S. B., Kjeldsen, H., Meibom, S., Morrison, D., Owen, T., Reitsema, H., Tarter, J., Bryson, S. T., Dotson, J. L., Gazis, P., Haas, M. R., Kolodziejczak, J., Rowe, J. F., Van Cleve, J. E., Allen, C., Chandrasekaran, H., Clarke, B. D., Li, J., Quintana, E. V., Tenenbaum, P., Twicken, J. D., and Wu, H., "Kepler Mission Design, Realized Photometric Performance, and Early Science," The Astrophysical Journal 713, L79-L86 (Apr. 2010). arXiv:1001.0268 [astro-ph].

[8] Johnson, J. A., Winn, J. N., Cabrera, N. E., and Carter, J. A., "A SMALLER RADIUS FOR THE TRANSITING EXOPLANET WASP-10b*," The Astrophysical Journal 692, L100 (Feb. 2009). Publisher: The American Astronomical Society.

[9] Fletcher, J., McQuaid, I., and Thomas, P., "Feature-Based Satellite Detection using Convolutional Neural Networks," in [AMOS], 11 (2019).

[10] Fitzgerald, G., Funke, Z., Cabello, A., Asari, V., and Fletcher, J., "Toward deep-space object detection in persistent wide field of view camera arrays," 13 (2021).

[11] Salvatore, N. and Fletcher, J., "Learned Event-Based Visual Perception for Improved Space Object Detection," 2888-2897 (2022).

[12] Cabello, A. and Fletcher, J., "SatSim: a synthetic data generation engine for electro-optical imagery of resident space objects," in [Sensors and Systems for Space Applications XV], Pham, K. D. and Chen, G., eds., 6, SPIE, Orlando, United States (June 2022).

[13] Felt, V. and Fletcher, J., "Seeing Stars: Learned Star Localization for Narrow-Field Astrometry," (2023).

[14] Gazak, J. Z., Johnson, J. A., Tonry, J., Dragomir, D., Eastman, J., Mann, A. W., and Agol, E., "Transit Analysis Package: An IDL Graphical User Interface for Exoplanet Transit Photometry," Advances in Astronomy 2012, e697967 (June 2012). Publisher: Hindawi.

[15] Tonry, J., Burke, B. E., and Schechter, P. L., "The Orthogonal Transfer CCD," Publications of the Astronomical Society of the Pacific 109, 1154-1164 (Oct. 1997). ADS Bibcode: 1997PASP..109.1154T.